The UA1 CENTRAL DETECTOR

M. Calvetti, P. Cennini, S. Centro, E. Chesi, S. Cittolin, A.M. Cnops, L. Dumps, D. DiBitonto, S. Geer, B. Haynes, W. Jank, G. Jorat, V. Karimaki, H. Kowalsky, R. Kinnunen, F. Lacava, G. Maurin, A. Norton, G. Piano Mortari, M. Pimia, A. Placci, P. Queru, M. Rijssenbeek, C. Rubbia, B. Sadoulet, K.S. Sumorok, C. Tao, V. Vuillemin, J.P. Vialle, H. Verweij and E. Zurfluh

UA1 Collaboration

Presented by M. Calvetti

Abstract

The UA1 Central Detector is now taking data at the CERN $p\bar{p}$ Collider[1,2]. We give a general description of the detector and discuss the aspects that are mainly related to its quality and reliability. Multi-hit electronics is used for the readout of 6000 sense wires uniformly distributed over 25 m^3. The analog information, energy, and charge division, is digitized on line every 32 ns. The high density and the precision of the points detected along the tracks is such that the reconstructed events look similar to bubble chamber pictures. Results obtained in the first physics runs are presented.

1. Introduction

The UA1 Central Detector is now installed and working at the CERN $p\bar{p}$ Collider (Fig. 1). An artist's view of the experimental set-up is shown in Fig. 2.

The magnet, a dipole with a nominal field value 0.7 T, has an internal magnetic volume of 80 m^3, of which 25 m^3 around the beam pipe are occupied by the central detector used for tracking and momentum measurement.

The complexity of the events produced by $p\bar{p}$ interaction at 540 GeV in the c.m., in terms of rates, multiplicity, and particle density, is such that a careful design of the detector geometry and of the associated electronics was needed. The construction of the detector and the basic features of the associated electronics have been described at the 1980 Vienna Conference on Wire Chambers[3,4].

We give here a general description of the detector, concentrating on the points which, on the basis of our experience, are fundamental to contributing to its final quality and reliability: i) geometry, ii) HV system, iii) electronics, iv) calibration.

2. Geometry

The expected topologies of $p\bar{p}$ interaction at 540 GeV in the c.m., where many particles with high energy are produced in the forward directions, suggested the use of a long detector with a magnetic field orthogonal to the beams.

The detector is composed of six independent half-moonshaped chambers assembled together to form a self-supporting cylinder, 6 m long and 2.2 m in diameter, covering the full solid angle from 5° to 175° with respect to the beam direction.

The cylinder is filled with a mixture of 60% ethane and 40% argon at atmospheric pressure.

The 6000 sense wires and the 17,000 field-shaping wires are parallel to the magnetic field. They are organized in horizontal planes in the four forward modules, and vertical planes in the two central ones (Fig. 3).

One of the most striking features of the system is the cylindrical shell of the chambers supporting the wires. It is a stressed honeycombed structure, 5 cm thick, sandwiched between two Vetronite layers, each 1.5 mm thick. The amount of prestressing, which, after wiring, is entirely counterbalanced by the tension given to the wires, is such that in the median plane the distance between the chamber edges is reduced by about 8 cm. The cylindrical shape, after wiring, depends on the equilibrium between the tension given to the wires and the stresses in the structure.

To measure the mechanical tension of the stretched wires, a simple, precise, and fast method, based on the measurement of the natural oscillation frequency, has been developed[5].

The sense wires (Ni-Cr, Ø 35 μm) and the field-shaping wires (Cu-Be, Ø 100 μm for VC-VF wires, 150 μm for cathode wires) were stretched to 80 g and 200 g, respectively. Figure 4 shows the results obtained for the 1000 sense wires in a module.

The position of the sense wires in a plane is known within 50 μm, whilst the position of the "average planes" in the 25 m^3 of the detector is known to an accuracy of 200 μm.

The sense wires are surrounded by field-shaping wires, as shown in Fig. 5. The VC voltage balances the electrostatic forces produced by the drift electric field onto the sense wires, whilst VF controls the gas amplification.

Electrons produced by the ionizing particles in the detector drift through large drift spaces (18 cm) to the anode wires, where the individual track coordinates are obtained by the drift time and charge-division method. With a drift field of 1.5 kV/cm, the drift velocity is 5.3 cm/μs and the maximum drift time 3.6 μs, smaller than the time interval between two successive bunch crossings (3.8 μs). When an interaction takes place, all the ionization (electrons) produced in the previous bunch crossing has already reached the anode wires.

The sagitta in the plane orthogonal to the magnetic field is measured with the drift time, which is far more precise than the charge division (two orders of magnitude). Figure 6 shows some events and the planes structure of the detector. The planes in the central modules are rotated by 90° to have the drift electric field orthogonal to the particle trajectories in the central region.

We can see how the detector "follows" the events, maintaining a constant density of points along the tracks all over the volume. These events were recorded during the November-December 1981 runs; at that time only 40% of the electronics was operational (80% of the sensitive volume). In particular, only one wire out of two was instrumented. With the complete electronics, an average of 100 points per track are recorded, each corresponding to 1 cm of gas sampling.

The high precision of the drift time coordinate, compared to the detector dimension, permits a good pattern recognition in the plane orthogonal to the magnetic field. The charge division coordinate corresponding to a specific hit is then easily reconstructed using the time information associated with the charge collected on both sides of the sense wires (see the section on Electronics).

3. HV system

The drift voltage (VD) applied to the drift volume needs to be degraded all along the edges of the drift space in order to guarantee planar equipotential surfaces. This is achieved with a resistor divider that feeds the tracks of a printed circuit, called "race-track" (RT), with decreasing voltages (Fig. 5). These

resistors are mounted inside the chambers and have a high total resistive value (3.5 GΩ).

It is then clear that any leakage current caused by the supporting structure of the chamber, or current due to the beam and collected by the RT, will drastically affect the potentials determined by the resistive chain, with an intolerable distortion of the electric field. It was therefore decided to connect the RT to 10 low-output impedance power supplies, so that any leakage or beam current would affect the electric field in only a small local region delimited by two power supply inputs. This is the role of the active divider[6].

The active divider is basically a number of vacuum tubes used as cathode followers connected in series. The maximum output current is roughly equal to the current flowing in the tube (1.5 mA) so that in the event of a short circuit the chain collapses, providing a simple means of current limitation. The voltages are fixed, with a precision of 0.5%, through a resistive divider connected to the grids.

For each drift volume, the currents associated with the intermediate voltages and with the field-shaping voltages VC and VF are measured in the power supplies, whilst the corresponding voltages are measured directly on the chambers. A total number of 308 currents and 308 voltages, corresponding to the 34 independent drift volumes (HV-wise) are continuously monitored by a SUPER CAVIAR computer[7] which also drives the HV power supply and controls the interlock logic (Fig. 7).

The ripple of the very high VD voltages (cathode) and of the 48 VC-VF voltage are also monitored through parallel wave-form recorders[8]. In case of HV troubles, the transients in all the HV lines are recorded. Careful study of these data turned out to be essential in understanding the behaviour of a detector which is usually inaccessible inside the magnet 200 m away from the control room.

In case of over-current (200 μA on VD, 50 μA on VC and VF, integration time about 1 ms) a hardware protection system[9] (Crowbar, Fig. 7) will disconnect the three (VD, VC, VF) voltages, associated with the same drift volume, in a few milliseconds. Furthermore, in order to avoid direct sparks from the HV race-track onto the wires, two HV transient suppressors (Transzorb)[10] are mounted on the chamber parallel to the first two intermediate voltages supplied by the active divider.

The VC-VF interlock system is composed of a general-purpose microprocessor controller (GPMC)[11] with a MOTOROLA 68B00 microprocessor with 64K EPROM and 2K RAM, which, with two special interface cards, controls the HV outputs and monitors the currents and voltages from the Crowbar boxes. It also controls the thresholds for the alarms and provides software filtering for them. The Crowbar boxes, where the HV relays are located, provide the current measurements through a floating current-to-frequency converter optocoupled to the low-level logic. In case of over-current, the GPMC can decide in a few hundred microseconds, whether to switch the chamber from the HV line to a shunt resistance. It also communicates with the SUPER CAVIAR responsible for the whole central detector activity.

4. Electronics

The block diagram of the electronics for each anode wire is shown in Fig. 8.

The two preamplifier signals at each end of the sense wire feed the charge and time digitizer (CTD)[4,12]. In the CTD (12 channels) there are 12 analog cards containing line receivers, clipping stages (32 ns), integrators, and 12 digital cards where the fast amplitude-to-digital converters (FADC, TRW-TDC1014J) and the memories are located. The analog chain is a.c. coupled. In order to avoid frequency dependence of d.c. offsets, a base line restorer has been introduced before the driver of the FADCs.

The two FADCs of each channel (six-bit accuracy, 32 ns sampling period) are used, respectively, as an analog divider to measure the ratio Q_i/Q_t (charge division) directly, and with a non-linear response for the measurement of the total energy Q_t in order to have the dynamic range (more than nine bits) required by Landau fluctuations. Every 32 ns the total charge collected Q_i and the hit coordinate along the wire Z_i are recorded.

The digital information is directly stored in successive memory locations in such a way that, at any time, the story of the previous 4 μs is recorded in the CTD memories (32 ns × 128).

The Z coordinate is given by the centre of mass of the Z_i's weighted by the energy E_i, measured in the same time bin

$$Z = \left(\sum Z_i \cdot E_i\right) / \left(\sum E_i\right) .$$

In order to have $Z = Z_{true}$ an infinite integration should be performed. In practice, a good measurement can be obtained with a gate width between 150 and 200 ns, depending on the pulse shape.

In the time channel there is a fine time-stop interpolator, a three-bit TDC of the DTR 247 type, which measures the drift time within a 32 ns window with an accuracy of 4 ns.

Five CTDs are located in each crate together with a readout processor (ROP)[13]. The data-acquisition system is described in another contribution to this conference (see S. Cittolin, UA1 Collaboration).

The electronics chain has been designed in such a way that it is limited, in the charge division accuracy, by the six bits of the FADC (1%). Figure 9 shows the charge division accuracy as a function of the total number of electrons collected on the wire. The stochastic noise of the wire resistance and of the preamplifier correspond to 1.2×10^4 r.m.s. electrons in a gate 150 ns long. In order to be limited in precision by the FADC, a total number of $\sim 4 \times 10^6$ electrons must be collected in 150 ns (five samples), requiring a gas amplification $\sim 10^5$.

The charge collected on one side of the wire depends dramatically on the position of the avalanche along the wire and on the Landau fluctuations. It is therefore essential for the analog part of the readout electronics to be linear over the full dynamic range (five times a minimum ionizing particle). The linearity of the analog chain has been measured by feeding calibrated charges into the preamplifier. Figure 10 shows $Z_{measured}$ versus $Z_{simulated}$ for a total energy corresponding to a minimum ionizing particle. The deviations from a linear fit to the data are always smaller than 1% all along the wire.

5. Calibration

The central detector electronics is provided with a calibration system (Fig. 11) which is able to feed into any preamplifier a variable charge up to five times a minimum ionizing particle with an accuracy of about 3%. The calibration pulse is obtained by the discharge of a 47 pF capacitor, previously charged to a reference voltage, through a 470 Ω resistance. Each preamplifier has its own RC.

The capacitors to be charged up are previously selected, using a set of serial shift registers HEF4015B. The trigger pulse, arriving at the same time on all the detectors, closes the c-mos switch SD 5100 thus causing the discharge of the capacitors. The shift register chain permits the 12,000 preamplifiers to be pulsed, with any required pattern and simulated charge division coordinate, i.e. two different reference voltages can be applied, one to the left and one to the right side.

A total of 730 pulsers, each driving 16 channels, are mounted directly on the chambers inside the connectors which at the same time support the preamplifiers and feed the VC-VF voltages to the field-shaping wires.

This flexible system, very useful as a debugging tool (in a few minutes we can check the layout and status of the electronics) is fundamental, in particular for the charge division calibration.

The measured charge division coordinate Z_m is related to the true one Z_t by the following expression:

$$Z_m = \frac{g_\ell Z_t + O_\ell/Q_{tot}}{(g_\ell - g_r)Z_t + g_r + O_{tot}/Q_{tot}}$$

where g_ℓ ang g_r are the left and right gains, and O_ℓ, O_{tot} are the d.c. offsets eventually present at the inputs of the two FADCs of the charge division and energy, respectively.

In order to control these offsets (1 mV corresponds to about 1% in Z) and avoid energy dependence of the charge division measurement, a set of six DACs, controlled by the ROP, are located on the analog card of each wire.

Using the calibration pulser, it is possible to simulate several positions along the wire for different energy losses. The two DACs controlling the left and right gains and those controlling the O_ℓ and O_{tot} offsets are changed by the ROP and chosen to have $(g_\ell/g_r) = 1$ and to minimize the offsets. Figure 12 shows the charge division linearity obtained before and after the on-line calibration.

Two other DACs are used for the energy FADC: the first to change the base-line (pedestal of the energy FADC), the second to control the response function of the energy measurement.

A SUPER CAVIAR computer controls the calibration system and the 530 CTDs by means of the 125 ROPs which are connected in series through an advanced data link controller[14]. Notice that the ADLC line can also be used during data taking, in spy mode, to read ROP statistics on data acquisition.

All the 6000 channels are calibrated in parallel. Figure 13 shows a computer display obtained using the calibration pulses to simulate a minimum-ionizing particle in the middle of the drift volume. The total energy (full histogram) and the charge division (continuous line) are shown for the 12 wires. Note how the charge division stays more or less constant in the time bins where the charge is collected, and how it deviates from the simulated position outside of the pulses where the noise is dominating.

The charge division linearities of the channels in a crate are shown in Fig. 14 (five CTDs, only one wire out of two was instrumented).

Other displays are used for debugging purposes. For instance, Fig. 15 shows the drift time, the energy base-line, the total energy, and the charge division obtained on 48 wires. It is clear that the broken channels can immediately be found. The relative T_0 due to different propagation times along the cables and to the readout electronics are measured with an accuracy of $\sim$ 4 ns. The energy measurements are equalized to the 10% level, well below the Landau fluctuations.

A second off-line calibration is then performed, but this time the corrections to the data are smaller than or comparable to the required accuracies.

6. Internal calibration and results

The electronics calibration cannot take into account the other parameters that contribute to chamber precision, such as absolute T_0's, drift velocity, drift angle, errors in the wire positions, and the relative positions of the six modules. To correct for these errors, we have to use other methods. There are two possibilities: either to simulate tracks in the detector, using X-rays or laser beams (see B. Sadoulet, this conference); or to use the tracks produced by real events to fit those parameters in order to obtain the best reconstruction.

The X-ray guns and the lasers of the UA1 detector are now being installed, and we do not have experimental results apart from tests on prototypes. To analyse the data taken in the last run, we have used the second method.

The chamber geometry, namely the way in which the planes are organized, is such that the "internal" calibration method can be fully exploited. This is due to the fact that the particles usually cross several drift volumes with different drift direction.

The errors in the drift angle, drift velocity, and absolute T_0 generate inclinations and displacements of the various track segments. It is then possible to tune the various parameters and choose the values that correspond to the best reconstruction. Using this method, the drift velocity and the drift angle have been measured independently in the six modules of the detector with a precision of 0.5%, and within this precision they are equal. The measured drift velocity is 53 μm/ns, whilst the drift angle is 22.2° (E = 1.2 kV/cm, B = 5.6 kG).

Figure 16 shows the residuals in the drift time coordinate obtained for different track categories: (a) to (c) show the residuals for tracks crossing one, two, and three drift volumes; the histogram (d) corresponds to tracks crossing different modules. The increase in error from 270 μm to 340 μm shows the presence, at this stage of the analysis, of systematic errors that will, of course, be corrected for.

The over-all precision obtained for all the reconstructed tracks in the 25 m^3 of the detector, in the presence of a 5.6 kG magnetic field, is shown in Fig. 17. A 290 μm accuracy is obtained.

In order to see whether systematic effects due to misalignment of the wire planes or wrong relative position of the six modules could introduce bias on the momentum measurement, we have fitted straight tracks (without magnetic field), using the normal reconstruction program used for events in a magnetic field. Any unknown deformation of the detector geometry is interpreted as curvature of the tracks; hence, in such a case, tracks with low momentum are reconstructed. Figure 18 shows the results. The vertical scale is the number of tracks (arbitrary units) and the horizontal scale is the ratio Q/p, where Q is the charge and p the momentum in GeV/c. The histogram is symmetric; no charge asymmetry in the momentum measurement is found.

We have also studied particle ionization using the dE/dx measurement[15]. The data were obtained by exposing one of the central detector modules to a 3 GeV/c muon beam. In Fig. 19 the Landau distribution based on 22,000 samples of energy loss measurements is shown. The absolute energy scale is calibrated using the 5.9 keV peak produced in Ar by an ^{55}Fe radioactive source. The data are corrected for the inter-channel cross-talk effect: 4% for the adjacent wires and 0.5% for the next two.

Each track was defined by 34 measured points. Figure 20 shows the mean ionization loss of the lowest 70% of the measurements on each track. The Gaussian fit to the distribution gives 1.4 keV for the average energy loss, with 0.16 keV standard deviation. An energy loss resolution of 6% is expected for tracks with 100 detected points. In Fig. 21 we show the prediction for the particle separability in units of standard deviations as a function of the momentum for pions, kaons, and protons. There is no separation between pions and kaons at 1.2 GeV/c nor between kaons and protons at 3 GeV/c. Above these points the separability increases quickly, reaching maximum values at 2-10 GeV/c and flattening out at high momenta.

The charge division accuracy has also been measured in this test in the beam. The results are shown in Fig. 22. A FWHM of 10 cm with 2.2 m long wires is found (σ = 2% of the wire length), compatible with the precision of our calibration system. At this stage of the analysis it is not possible to present definitive results on the charge division accuracy obtained in the reconstructed $p\bar{p}$ interactions. The data have been taken two

months ago and the complete reconstruction program was attempted recently. We will produce these results in the very near future.

7. Conclusions

In spite of its simplicity, the detector geometry, coupled with the magnetic field, is well adapted to the event structure; drift volumes with opposite electric fields provide a unique tool for internal calibration (drift velocity, drift angle, T_0).

To avoid risks, a highly sophisticated HV system has been provided. Currents and voltages are monitored, and a hardware protection (Crowbar) must run continuously to avoid multiple sparks inside and outside the detector. The capacitor monitors, read by the wave-form recorders, turned out to be the most simple and direct way of following the HV activity of the detector.

The flexibility and completeness of the HV system is essential for the remote control of such a complex detector. Because of their complexity, all the UA1 central detector components (high voltages, low voltages, calibration electronics, readout electronics, gas system, cooling system of the preamplifiers, temperature measurement all over the detector surface) are controlled by computer. A sophisticated and complete software has been written.

The use of the FADC as a wave-form recorder is a powerful and relatively simple instrument for drift chamber readout, especially for events with a high particle density when the pulse shape has to be used to distinguish the various components in a narrow jet.

We have 300 μm accuracy in the drift time coordinate with magnetic field all over the detector volume. An energy resolution of 6% is expected, using the truncated mean for particles with 100 detected points. The charge division accuracy is measured to be around 3%, compatible with the precision of our calibration system. No internal calibration has yet been attempted on the charge division. The analysis is still in a preliminary stage and there is room for further improvements.

References

1. Staff of the CERN $\bar{p}$-p project, Phys. Lett. 107B (1981) 306.
2. G. Arnison et al., Phys. Lett. 107B (1981) 320.
3. M. Barranco-Luque et al., Nucl. Instrum. Methods 176 (1980) 175.
4. M. Calvetti et al., Nucl. Instrum. Methods 176 (1980) 255.
5. M. Calvetti et al., Nucl. Instrum. Methods 174 (1980) 285.
6. E. Chesi, CERN $\bar{p}$-p Tech. Note 81/17 (1981).
7. S. Cittolin and B.G. Taylor, Proc. Topical Conf. on the Application of Microprocessors to High-Energy Physics Experiments, CERN 81-07, p. 533.
8. S. Centro, private communication ($\bar{p}$-p Tech. Note to be published).
9. D. DiBitonto et al., CERN $\bar{p}$-p Tech. Note 82/07 (1982).
10. C. Rubbia, CERN $\bar{p}$-p Tech. Note 80/21 (1980).
11. S. Centro and V. Vuillemin, $\bar{p}$-p Tech. Note 80/81.
12. B. Hallgren and H. Werweij, IEEE Trans. Nucl. Sci. NS-27 (1980) 333.
13. S. Cittolin and B. Löfstedt, Proc. Topical Conf. on the Application of Microprocessors to High-Energy Physics Experiments, CERN 81-07, p. 91.
14. S. Cittolin, B. Löfstedt and E. Zurfluh, Topical Conf. on the Application of Microprocessors to High-Energy Physics Experiments, CERN 81-07, p. 573.
15. R. Kinnunen, CERN $\bar{p}$-p Tech. Note 81/30 (1981).

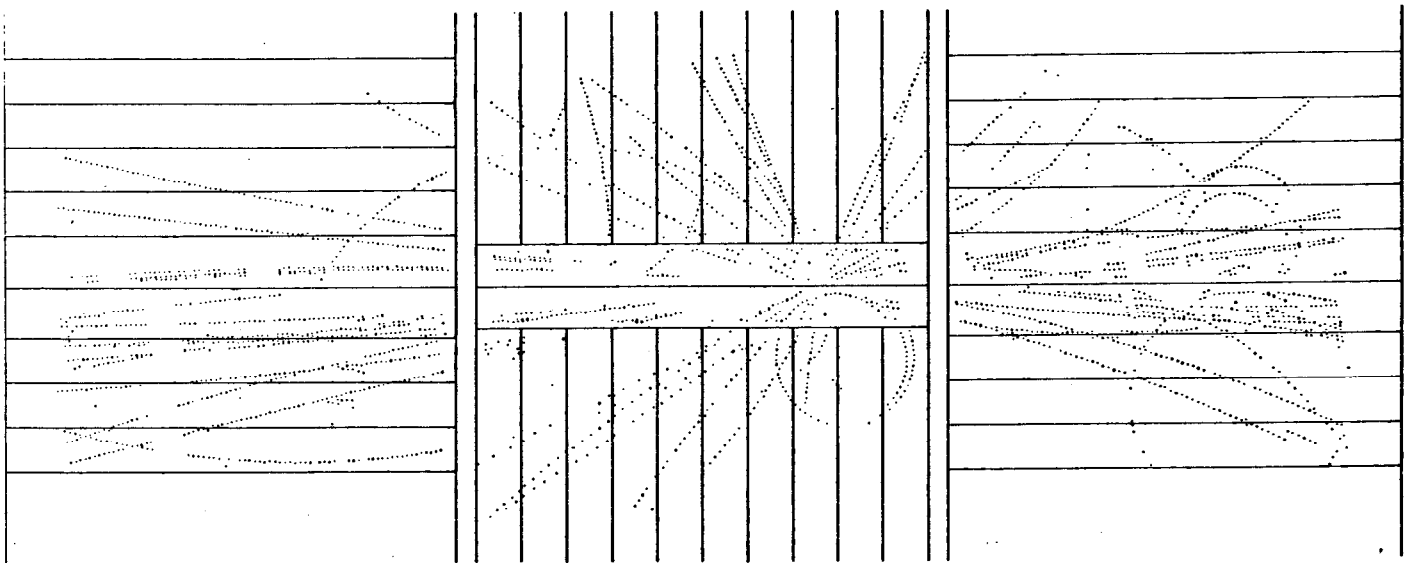

Fig. 1 Proton-antiproton interaction at 540 GeV in the centre of mass

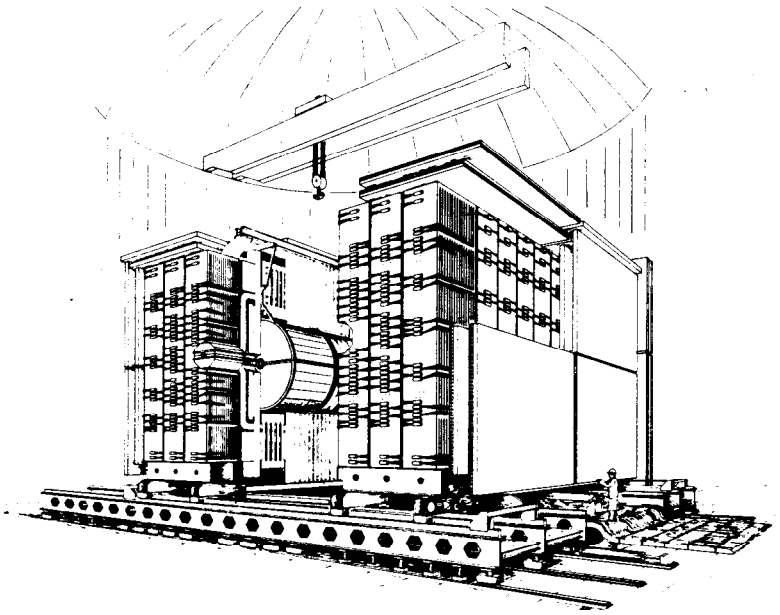

Fig. 2 The UA1 experimental apparatus working at the CERN $p\bar{p}$ Collider

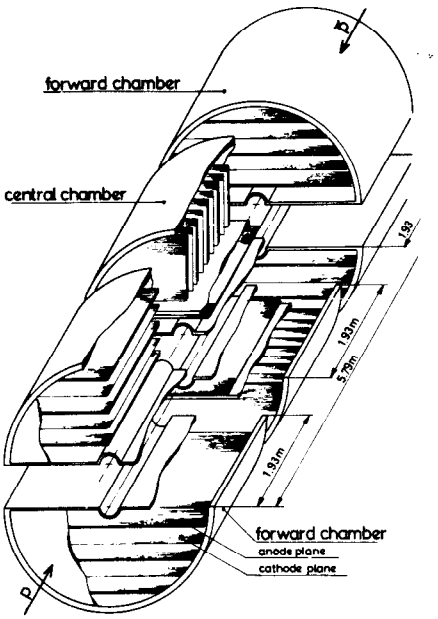

Fig. 3 The UA1 Central Detector. This is composed of six independent modules assembled to form a cylinder around the vacuum pipe.

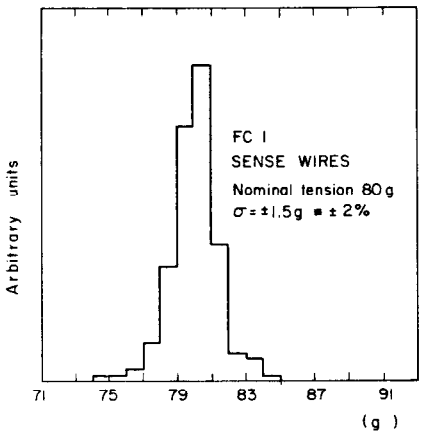

Fig. 4 Typical distribution of the mechanical tension for all sense wires in a module (∿ 1000 wires)

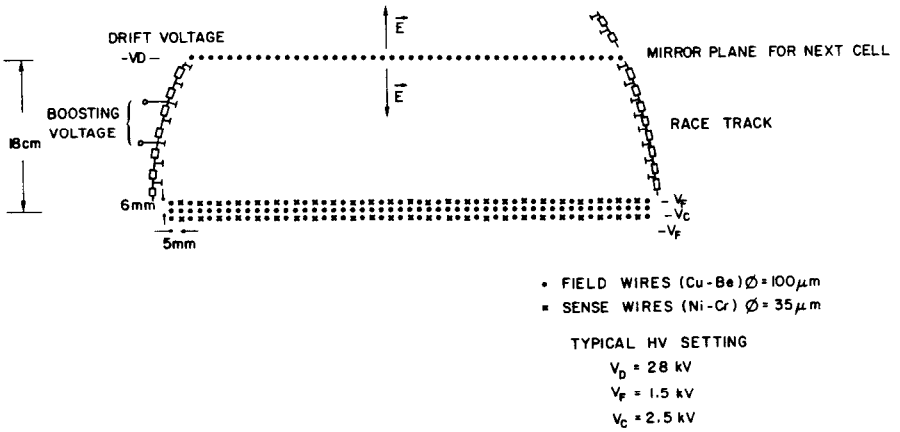

Fig. 5 Drift cell of a forward chamber

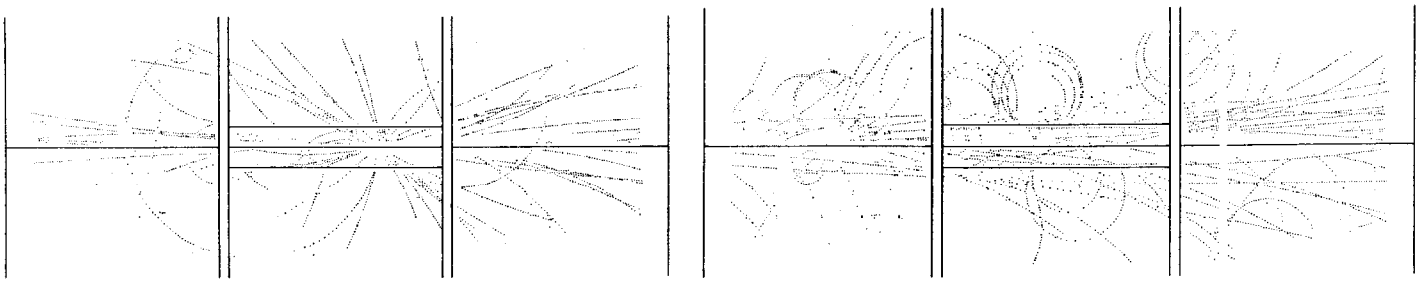

a) Proton-antiproton interaction at 540 GeV.

b) Beam-gas interaction.

Fig. 6

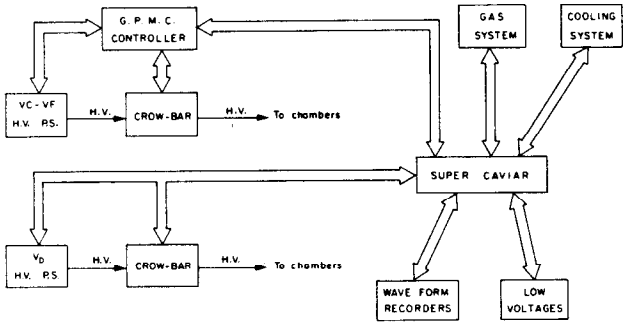

Fig. 7 Block diagram of the interlock system

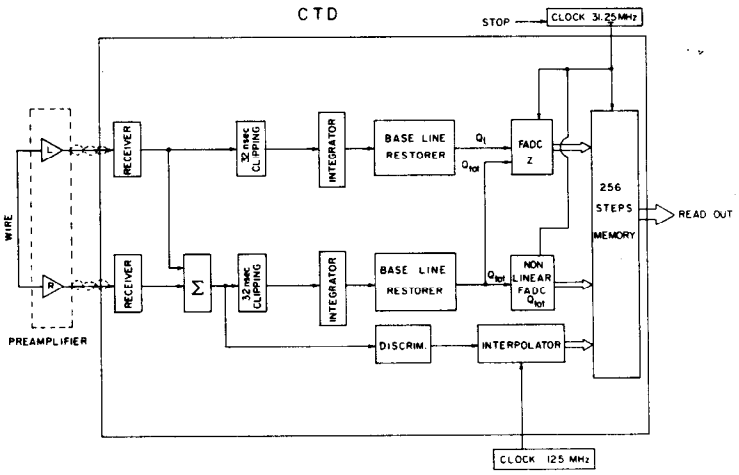

Fig. 8 Block diagram of the electronics associated with each wire

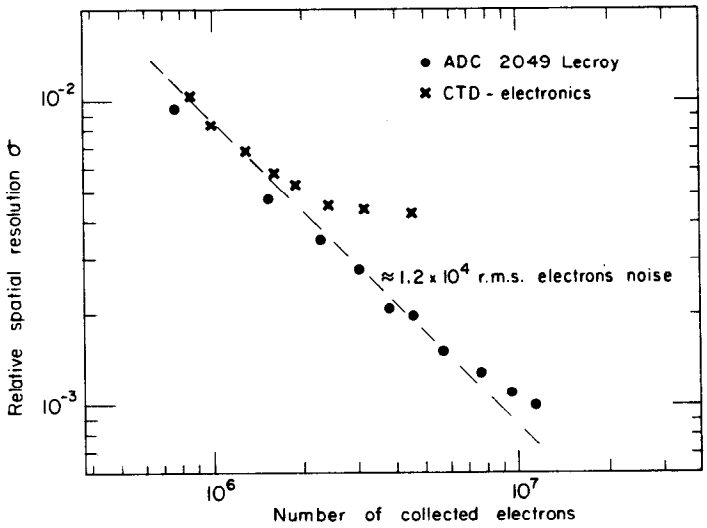

Fig. 9 Charge division accuracy versus number of electrons collected on the wire, in a 150 ns gate.

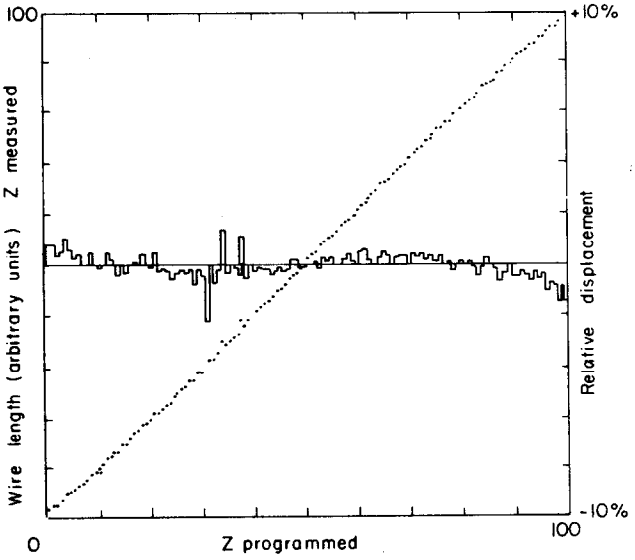

Fig. 10 Linearity of the analog chain

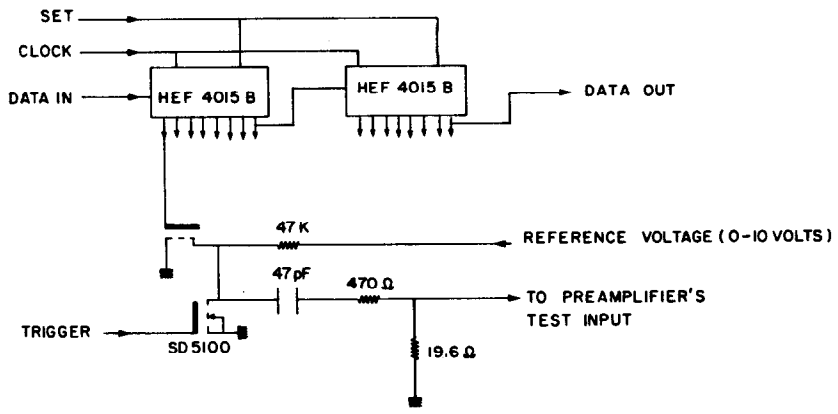

Fig. 11 Calibration pulser associated with each preamplifier

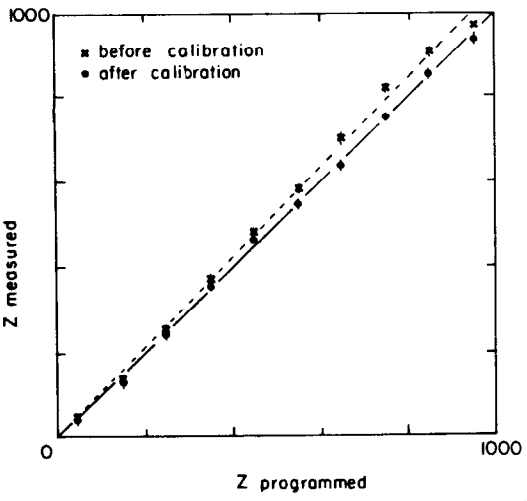

Fig. 12 Charge division linearity before and after the on-line calibration

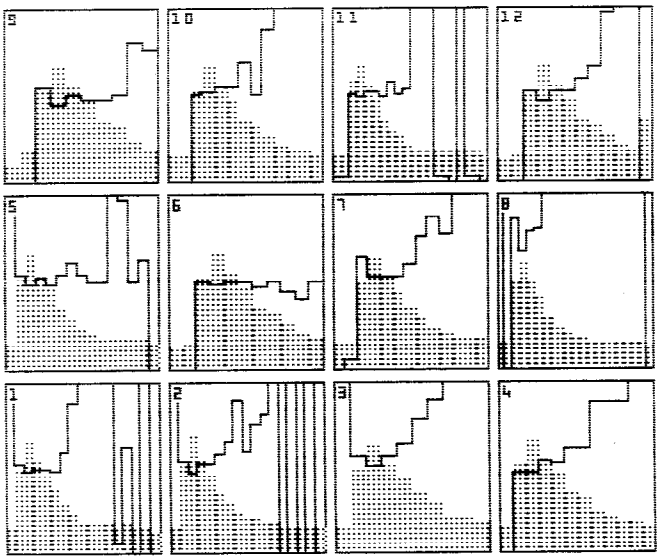

Fig. 13 Calibration pulses simulating a minimum ionizing particle on 12 wires in a CTD module. The total energy (full histogram) and the charge division (continuous line) are measured every 32 ns (32 ns/bin). The vertical scale 0-63 corresponds to the six bits of the FADCs.

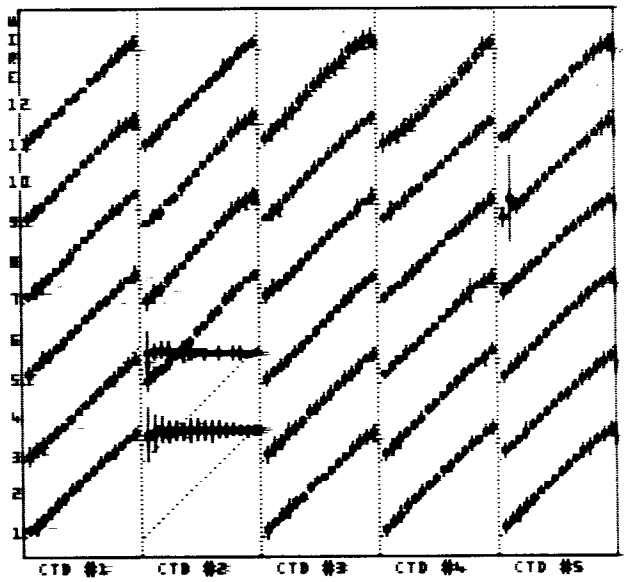

Fig. 14 Charge division linearities of the channels in a crate (five CTDs; only one wire out to two was instrumented).

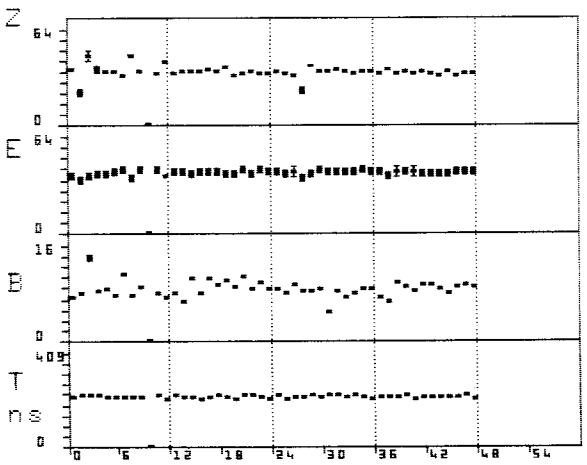

Fig. 15 Drift time, energy base line, total energy, and charge division obtained on 48 wires with the calibration pulser

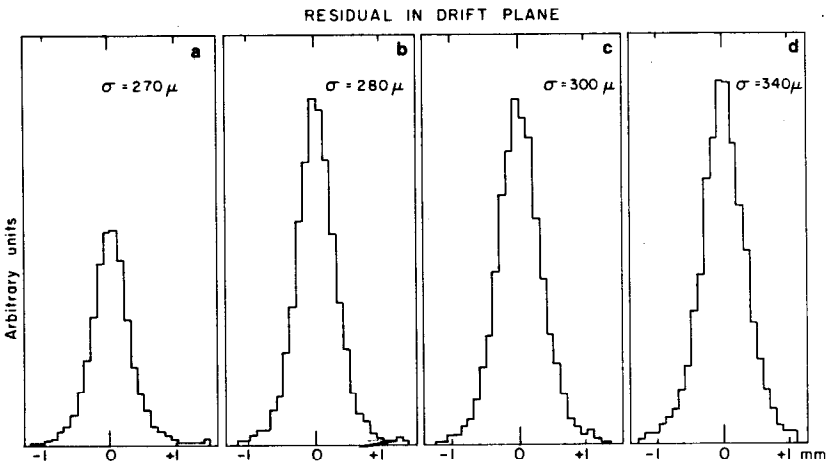

Fig. 16 Drift time residuals for different track categories: a) particles crossing one drift volume; b) particles crossing two drift volumes; c) particles in a complete chamber; d) particles crossing different chambers.

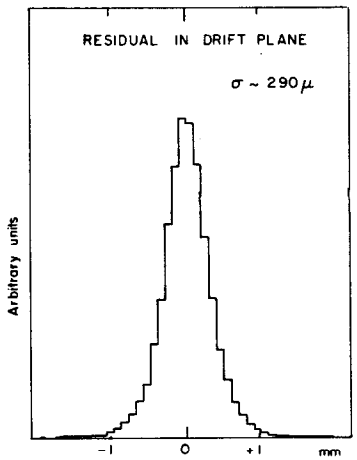

Fig. 17 The over-all precision obtained for all the reconstructed tracks in the 25 m^3 of the detector in the presence of a 5.6 kG magnetic field

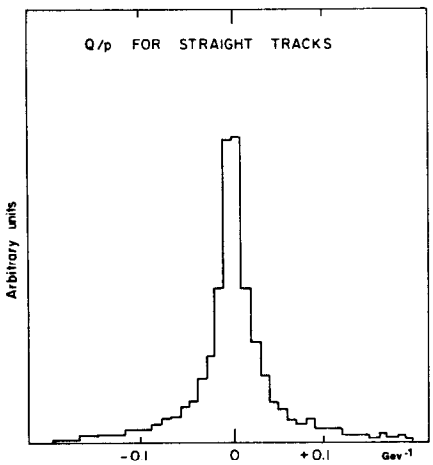

Fig. 18 Measured momentum of straight tracks (data taken without magnetic field). The symmetry of the histogram shows that there is no geometrical distortion in the momentum measurement.

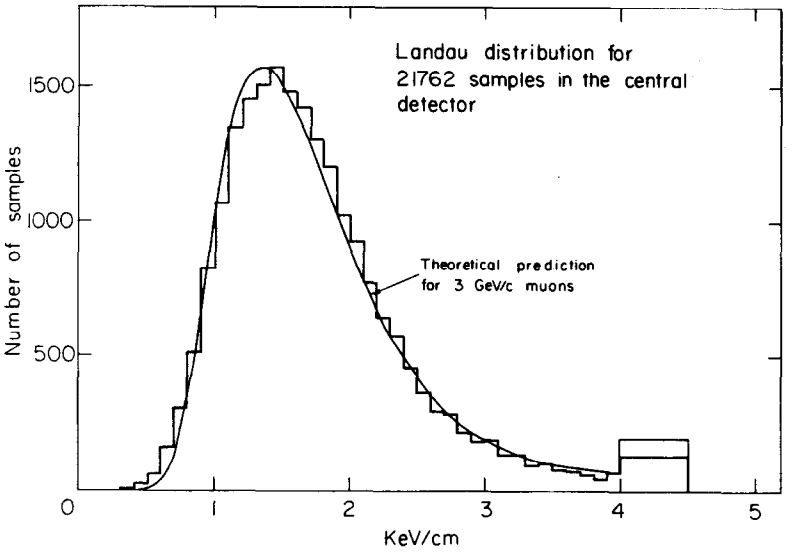

Fig. 19 Landau distribution of the measured energy losses

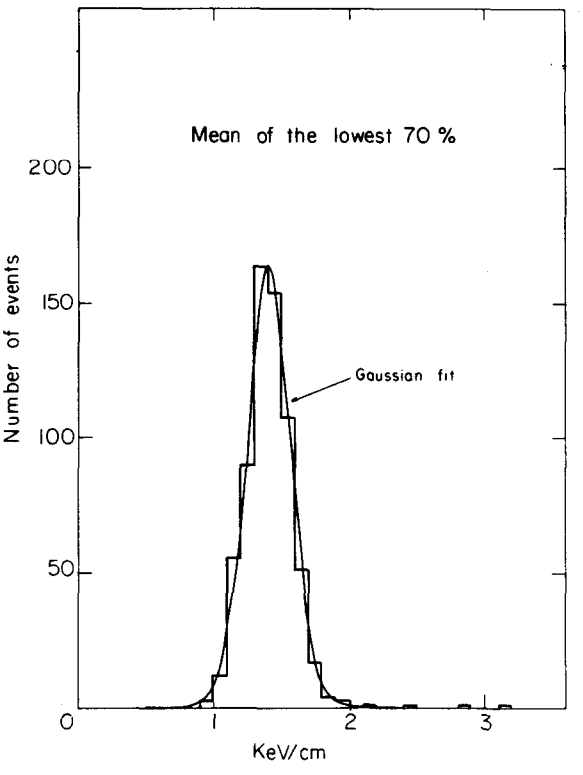

Fig. 20 Truncated mean of the energy losses, i.e. mean, from 34 samples of 1 cm each, of the 70% which are lowest in energy.

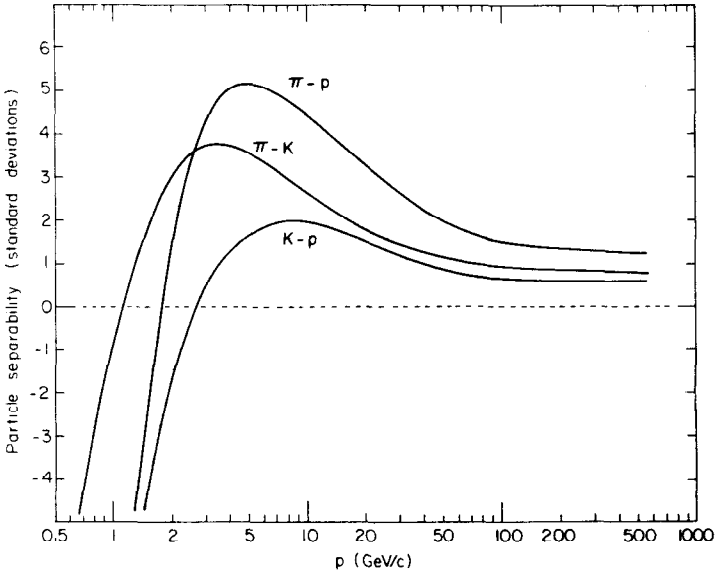

Fig. 21 Expected particle separability in units of standard deviations as a function of the momentum for pions, kaons, and protons.

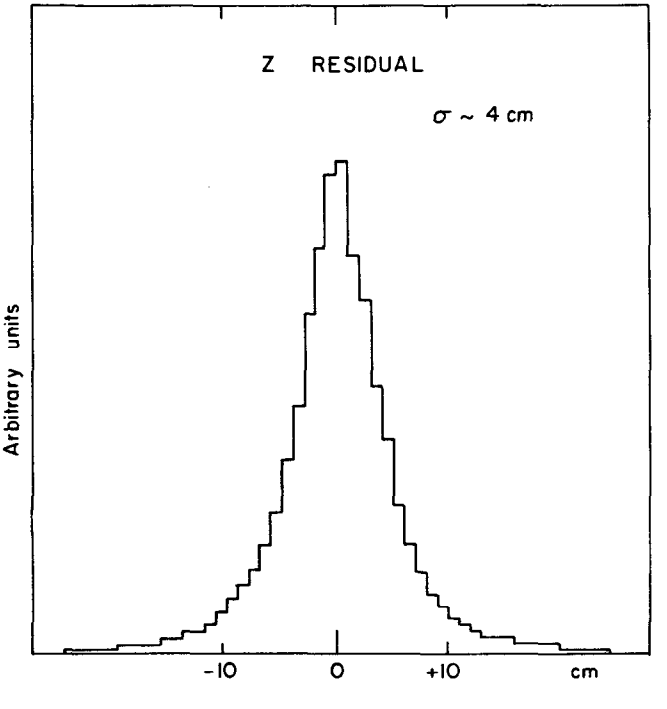

Fig. 22 Charge division accuracy obtained at the very early stage of the analysis. Optimization of the gas amplification and off-line calibration procedure has still to be performed.